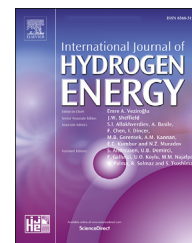




ELSEVIER

Available online at [www.sciencedirect.com](http://www.sciencedirect.com)

ScienceDirect

journal homepage: [www.elsevier.com/locate/he](http://www.elsevier.com/locate/he)

# Numerical investigations of mixed supersonic and subsonic combustion modes in a model combustor

Zhiwei Huang, Huangwei Zhang\*

Department of Mechanical Engineering, Faculty of Engineering, National University of Singapore, 9 Engineering Drive 1, Singapore, 117576, Singapore

## HIGHLIGHTS

- Three methods are proposed to quantify the supersonic and subsonic combustion modes.
- Probability distributions of supersonic and subsonic combustion modes are presented.
- Critical global equivalence ratio for thermal choking of supersonic inflow is derived.
- Flame lift-off distance in both supersonic and subsonic flows are quantified.

## ARTICLE INFO

### Article history:

Received 28 August 2019

Received in revised form

22 October 2019

Accepted 25 October 2019

Available online xxx

### Keywords:

Supersonic combustion

Combustion mode

Mach number

Heat release

Thermal choking

Global equivalence ratio

## ABSTRACT

Flame dynamics and statistics of mixed supersonic and subsonic combustion modes under different air inflow and global equivalence ratio conditions in a hydrogen-fueled model combustor are numerically studied. Three methods including spanwise-averaged Mach number, spanwise-averaged Mach number conditioning on the local heat release, and fraction of heat release are proposed to identify supersonic and subsonic combustion modes. The probability distributions of supersonic and subsonic combustion modes are also analyzed based on the statistics on multiple instantaneous snapshots of the numerical results. The critical global equivalence ratio for thermal choking in a range of supersonic inflow conditions is derived theoretically based on a one-dimensional duct flow with heat addition. Furthermore, it is found that the flame lift-off distance in both supersonic and subsonic flows decreases with increased air inflow velocity, but increases with global equivalence ratio. The fraction of supersonic heat release and its oscillation increase with increased air inflow velocity.

© 2019 Hydrogen Energy Publications LLC. Published by Elsevier Ltd. All rights reserved.

## Introduction

The combustion physics under supersonic inflow conditions are significant topics in the design and development of scramjets [1]. Mach number ( $Ma$ ) of main flow in the combustor increases with increased flight Mach number and eventually the gas remains supersonic throughout the combustor. Intuitively, it is easier to achieve supersonic

combustion at higher inflow Mach numbers, lower global equivalence ratios, and smaller recirculation zones resulting from bluff-body type flameholders [2]. However, local subsonic flow regions may also result from the following possible factors: (a) flame stabilization devices, e.g. cavity, strut and pylon, leading to locally low-speed recirculation zones [3,4]; (b) large global equivalence ratios (larger than the critical value for thermal choking) in engineering practices to achieve enough engine thrust, which may

\* Corresponding author.

E-mail address: [huangwei.zhang@nus.edu.sg](mailto:huangwei.zhang@nus.edu.sg) (H. Zhang).

<https://doi.org/10.1016/j.ijhydene.2019.10.193>

0360-3199/© 2019 Hydrogen Energy Publications LLC. Published by Elsevier Ltd. All rights reserved.

Nomenclature	
<b>Symbols</b>	
$Ma$	Mach number
$\delta(x)$	Dirac delta function
$A_f$	frequency factor
$A, B, C$	PDF of supersonic/subsonic/no flamelet
$n$	temperature exponent
$P_{ijk}$	spatial position in the domain
$E_a$	activation energy
$n$	number of samples used
$a_F, b_O$	reaction orders for F/O
$a_{ijk}, b_{ijk}, c_{ijk}$	number of supersonic/subsonic/no flamelet at point $P_{ijk}$
$[F], [O]$	concentrations of F/O
$e_{ijk}$	sum of $\xi_{Ma-q}$ at point $P_{ijk}$
$T^*$	stagnation temperature
$f_{ijk}$	sum of $ \xi_{Ma-q} $ at point $P_{ijk}$
$p$	static pressure
$A_{ijk}, B_{ijk}, C_{ijk}$	PDF of supersonic/subsonic/no flamelet at point $P_{ijk}$
$\varphi$	global equivalence ratio
$\bar{\xi}_{Ma-q}$	average of $\xi_{Ma-q}$
$Ma_c$	convective Mach number
$\sigma_{\xi_{Ma-q}}$	standard deviation of $\xi_{Ma-q}$
$u_x$	stream-wise velocity
$\varphi_{cr}$	critical $\varphi$ for thermal choking
$Y_i$	mass fraction of species $i$
$\rho$	density
$\dot{q}$	heat release rate per unit volume
$S$	area of the cross-plane
$\xi_{Ma}$	a binarized metric identifying supersonic/subsonic flows
$k$	specific heat ratio
$max, min$	maximum/minimum functions
$\dot{q}_{loss}$	rate of heat loss
$sign$	sign function
$c_p$	heat capacity
$\xi_{Ma-q}$	$\xi_{Ma}$ conditioning on local HRR
$R$	gas constant
$\bar{q}$	volume average of $\dot{q}$
$a$	speed of sound
$\beta$	threshold fraction to extract non-negligible $\dot{q}$
$\dot{Q}_{cr}$	critical $\dot{Q}$ for thermal choking
$z_{st}$	stoichiometric mixture fraction
$\dot{m}_{H_2}, \dot{m}_{air}$	mass flow rates of $H_2$ /air
$\overline{Ma}$	spanwise-averaged Mach number
LHV	lower heating value
$L_y$	a line in the $y$ -direction
$x_0$	axial location of the strut base
$\overline{Ma}_{\bar{q}}$	$\overline{Ma}$ conditioning on local HRR
$c_{p,1}, c_{p,2}$	heat capacity at combustor entrance/exit
$L_y(\dot{q} \geq \bar{q} \cdot \beta)$	$L_y$ satisfying $\dot{q} \geq \bar{q} \cdot \beta$
$T_1^*, T_2^*$	stagnation temperature at combustor entrance/exit
$\dot{q}_{sup}, \dot{q}_{sub}$	$\dot{q}$ in supersonic/subsonic flows
$s$	stoichiometric mass ratio of F/O
$[\dot{q}_{sup}], [\dot{q}_{sub}]$	fractions of $\dot{q}_{sup}/\dot{q}_{sub}$ in $\dot{q}$
$Y_F^0, Y_O^0$	mass fractions of F/O in the F/O streams
$L_y(Ma \geq 1)$	$L_y$ satisfying $Ma \geq 1$
$Ma_1$	air inflow Mach number as a variable
$L_y(Ma < 1)$	$L_y$ satisfying $Ma < 1$
$U_{x1}$	air inflow velocity as a variable
$\dot{Q}$	volume integrated $\dot{q}$
$\dot{\omega}_{H_2}$	reaction rate of $H_2$
$\dot{Q}_{sup}, \dot{Q}_{sub}$	volume integrated $\dot{q}_{sup}/\dot{q}_{sub}$
$x_{FB}$	axial location of the flame base
$[\dot{Q}_{sup}], [\dot{Q}_{sub}]$	fractions of $\dot{Q}_{sup}/\dot{Q}_{sub}$ in $\dot{Q}$
$d_{lift-sup}^U, d_{lift-sub}^U$	upper branch of $d_{lift-sup}/d_{lift-sub}$
$\eta_g$	combustion efficiency
$d_{lift-sup}, d_{lift-sub}$	lift-off distance of supersonic/subsonic flame base
$P(\xi_{Ma-q})$	PDF of $\xi_{Ma-q}$
<b>Acronym</b>	
1D, 2D, 3D	one-, two-, three-dimensional
HRR	heat release rate
DLR	German Aerospace Center
PDF	probability density function

induce wall boundary layer separation due to large adverse pressure gradients [5,6]; (c) transverse or inclined fuel injections, which may also cause boundary layer separation [7,8]. Furthermore, the local recirculation zone, in which the gas flows and reacts under subsonic speeds has been proved important for reactant mixing and global flame stabilization in the supersonic main flows [9]. Flow disturbance, flame oscillation or even combustion instability may be generated, which may propagate upstream in subsonic flows and downstream in both supersonic and subsonic flows [10,11]. However, the mixed supersonic and subsonic flame dynamics under high-speed combustion conditions are still not well understood.

It is well acknowledged from experimental tests [12–14], numerical simulations [1,11,15,16], as well as theoretical analyses [17] that supersonic combustion of hydrogen is feasible in a

reasonable distance after injection. However, the implication is that combustion really takes place in supersonic flows. For the other studies on dual-mode combustors [2,12,18–21], the occurrence of mode transition is identified based on the experimentally measured wall pressure and the correspondingly estimated streamwise one-dimensional (1D)  $Ma$ , the optical visualizations like the high-speed flame image, the schlieren photograph or interferogram. Mach number at the combustor entrance [22], the maximum pressure rise in the combustor [23], and the sudden pressure rise upstream of the injector [24] are also used to identify the combustion mode. On the engineering aspect, the combustion modes can be only roughly estimated using these methods as they only take use of some global quantities, e.g. dispersive wall pressure,  $Ma$  at the combustor entrance. However, they are not sufficient for the real-time identification and precise control of mode transition in flight

tests or ground experiments. The spatial-nonuniformity and time-variation characteristics of the three-dimensional (3D) combustion field under supersonic inflows are neglected. On the scientific aspect, there are still some issues need to be clarified, e.g. whether it is reliable to identify the combustion mode based on the limited dispersive wall pressure or the simplified estimation of 1D  $Ma$  [2,18,19].

The thermal choking effect and the shock wave motion in the combustor are tightly related to the mode transition between supersonic combustion and subsonic combustion [25]. The incipient thermal choking and the stabilization of shock-train in the heat release region of the HyShot II scramjet are studied both experimentally and numerically by Laurence et al. [5,6]. The shock-train moves towards the rear of the combustor with increased equivalence ratio, however, not continuously. It is slowed and tends to be quasi-stable in a certain range of equivalence ratio, which is contrary to a simple Rayleigh-type choking analysis. The evolution of flame front relative speed is calculated based on experimental measurements on combustion iso-luminosity contours in a cavity-based supersonic combustor [26]. However, no information about flame front movement in supersonic and subsonic flows is extracted. Numerical simulations on mode transition are also performed in Refs. [27,28], and substantial progresses have been made in engineering application. Although they provide more detailed information than the experiments, however, the location of thermal choking and different combustion modes are still not quantified. The statistics of supersonic and subsonic combustion modes in space, the flame oscillation and heat release characteristics in supersonic and subsonic flows are still not fully understood yet [5]. Therefore, further investigations on the feasibility and extent of supersonic combustion, the statistics and instantaneous flame base movement and the heat release fraction in supersonic and subsonic flows are required from some other perspectives.

In this work, we aim to study some quantified flame dynamics and statistics in a mixed supersonic and subsonic combustion field. A model combustor in DLR (German Aerospace Center) is selected as the target configuration, which has been investigated by many researchers [11,29–36]. The measurements made by Waidmann et al. [37] is chosen as the base case, based on which a series of cases with different air inflow and global equivalence ratio conditions are proposed to study the variable combustion modes. The rest of the paper is organized as follows. Numerical models, including the discretization schemes and chemical kinetics are described in Section Numerical models. Physical models, i.e. the computational configuration, the mesh methodology, and the operating conditions are presented in Section Physical models. Results are analyzed in Section Results and discussion, and conclusions are drawn in Section Conclusions.

## Numerical models

### Numerical solver and discretization schemes

The governing equations for fully compressible reacting flows include the conservation laws of mass, momentum, energy, and species mass fractions [38]. A density-based, multi-

component, reactive solver *RYrhoCentralFoam* is developed based on a fully compressible flow solver, *rhoCentralFoam*, in OpenFOAM 5.0 package [39]. It is able to capture shock waves with low oscillation and dissipation using semi-discrete Kurganov–Tadmor central-upwind scheme [40,41]. The solver has been validated with supersonic flow and detonative combustion [42]. The similar *rhoCentralFoam*-based strategy has also been used by other groups, e.g. by Wu et al. [34] and Li et al. [32], for the supersonic hydrogen flames in the same DLR combustor, in which the velocity, pressure and overall flame behaviors are predicted reasonably well.

The governing equations are solved by cell-centered finite volume method. Implicit second-order Crank-Nicolson scheme is applied for the time discretization. The convective fluxes are reconstructed using a second order (flux limiter based) Gauss integration scheme with linear interpolation. The diffusive terms are split into orthogonal and non-orthogonal part to minimize the non-orthogonality error. The second-order Gauss scheme with linear interpolation is used for the orthogonal part and surface interpolation of variable normal gradients is applied for the non-orthogonal part [43]. The maximum CFL (Courant-Friedrichs-Lewy) number is set to be 0.3, which approximately corresponds to the physical time step of 10 ns. After sufficiently long initial calculations, more than 50 flow-through time (estimated from hydrogen bulk velocity and the combustor length), i.e. approximately 9.6 ms, are collected for statistical analysis in the following.

### Chemical kinetics

One-step irreversible reaction is used to describe the oxidation of hydrogen [44]. The reaction step with kinetics parameters for  $H_2/O_2$  are listed in Table 1, including frequency factor  $A_f$ , temperature exponent  $n$ , activation energy  $E_a$ , and reaction orders  $a_f$  and  $b_o$  with respect to the corresponding fuel and oxidizer, respectively. The reaction rate is calculated using the Arrhenius form, i.e.

$$\dot{\omega} = A_f T^n \exp(-E_a / RT) [F]^{a_f} [O]^{b_o}, \quad (1)$$

where  $[F]$  and  $[O]$  are the concentrations of the fuel and oxidizer, respectively.

The global reaction for hydrogen oxidation has been validated with the experimental data in terms of laminar flame speed, which shows good agreement for equivalence ratios ranging from 0.55 to 1.1 [44]. This mechanism is also used by Ingenito et al. [45], Gerlinger et al. [46], and Fureby et al. [47] for modelling supersonic combustion and it is found that the main combustion characteristics (e.g. wall pressure and temperature predictions [45], laminar flame speed [46], and flame stabilization [47]) are well captured. Furthermore, compared with our previous investigations on this combustor using 3D LES with detailed chemistry of 9 species and 27

**Table 1 – Reaction for  $H_2/O_2$  and kinetic parameters (units in cm-sec-mole-cal-Kelvins).**

Reaction	$A_f$	$n$	$E_a$	$a_f$	$b_o$	Reference
$2H_2 + O_2 \Rightarrow 2H_2O$	$4.74 \times 10^{12}$	0.0	10063.8	1.0	0.5	[44]

reactions (hereafter denoted as 9s/27r) [11,35], this global mechanism reproduces quite well for most features, e.g. temperature and Mach number, both instantaneously and statistically. The shock waves, expansion fans, and central combustion zones do not show fundamental differences compared with those obtained from the 9s/27r detailed mechanism. Therefore, this mechanism is expected to be sufficient for our current investigations since the emphasis is laid on the mixed combustion modes, instead of the finite-rate chemistry, in a model combustor configuration.

## Physical models

### Computational configurations and meshes

The hydrogen-fueled strut combustor [37] experimentally measured in DLR will be investigated in this work. Its two-dimensional schematic is shown in Fig. 1. Based on the previous work on the same combustor [11,29–36], it has been found that the interactions between the originally 15 circular fuel injectors are relatively small, and the major flow structures show quasi-two-dimensional (2D) characteristics. This is particularly true for the shocks, expansion fans and shear layers between the central recirculation zone and the high-speed air inflows. Therefore, 2D approximation is widely adopted in the simulations of this combustor, and one can see that results from the 2D computational domain well reproduce the main flow and combustion characteristics observed from experiments, including various zones of the recirculating flames as well as the lift-off distances [11,29–36]. Therefore, in this work we will also use the 2D domain to investigate the supersonic and subsonic combustion modes, which can considerably reduce the computational cost and make parametric studies affordable with high grid resolution. Compared with our previous investigations on this DLR combustor using 3D LES with one equation eddy viscosity turbulence model [11,35], the 2D simulations in this study well reproduces the main flow and combustion characteristics observed from experiments.

As shown in Fig. 1, the combustor is 50 mm in height (i.e.  $y$ -direction) at the entrance and 340 mm in length (i.e.  $x$ -direction). The strut is 32 mm in length and 6 mm in height. It is placed along the centerline of the combustor at 77 mm downstream to the entrance [37], and its rear lies at  $x = 109$  mm (as indicated in Fig. 1). The upper wall has a divergence angle of  $3^\circ$  since  $x = 100$  mm (indicated in Fig. 1) to compensate for the boundary layer expansion. At the rear of the strut, the fuel hydrogen is discharged through 15 circular

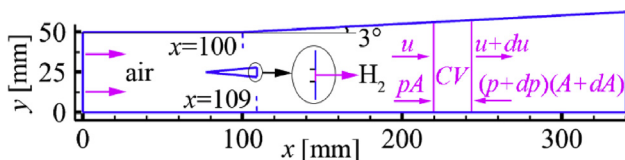


**Fig. 1 – Two-dimensional schematic of the DLR combustor [37]. The control volume is schematically shown for the analysis in Section Critical conditions for thermal choking.**

injectors (each 1 mm in diameter). Nevertheless, in our 2D simulations, these multiple circular injectors are simplified into a single slot (see the inset of Fig. 1). To ensure the global equivalence ratio and injection speed of hydrogen consistent with those used in the experiments, the width of the fuel slot is adjusted to be 0.3 mm. This similar treatment is also adopted by Wu et al. [34].

Three meshes with 55,800, 220,925, and 491,700 structured cells (denoted as M1, M2, and M3, respectively) are adopted to discretize the computational domain of the DLR combustor shown in Fig. 1. The grid dependence analysis and numerical validation with the above three meshes are provided in Appendix A. In general, the results obtained from mesh M2 are acceptable, through comparing the experimental data statistics of velocity and temperature. Therefore, mesh M2 will be chosen for the following analysis in Section Results and discussion. Note that the minimum grid size of mesh M2 is 0.06 mm in  $y$ -direction, and 0.14 mm in  $x$ -direction, respectively. This resolution is comparable with the work of Wang et al. [31] and Wu et al. [34], and therefore is expected to be sufficient for our current analysis.

### Simulation conditions

One base case (termed as Case-AB hereafter) is selected from the experimental measurements from DLR and the operating conditions are detailed in Table 2 [37]. Specifically, the air enters the combustor at  $2.0 Ma$  with a total temperature ( $T^*$ ) of 600 K and a static pressure ( $p$ ) of 0.1 MPa, respectively. It should be highlighted that the hot air is vitiated with  $H_2O$  addition (3.2% in mass fraction, see Table 2). The pure hydrogen is injected sonically with a total temperature ( $T^*$ ) of 300 K and a static pressure ( $p$ ) of 0.1 MPa. The global equivalence ratio ( $\phi$ ) is 0.034. The convective Mach number associated with fuel/air streams is defined as  $Ma_c = |(U_1 - U_2)/(c_1 + c_2)|$ , in which  $U_1$  and  $U_2$  are the inflow velocities of the two streams while  $c_1$  and  $c_2$  are the corresponding speeds of sound [48]. It describes the effects of compressibility on the development of mixing layers due to the two streams.

It is well known that the formation of supersonic or subsonic combustion is influenced by the air inflow velocity and/or fuel heat release. Higher inflow velocity and/or lower heat release may result in higher fraction of supersonic combustion [45,49]. At the fixed inflow Mach number, the inflow velocity of air depends on its total temperature, which also affects the reactant chemical kinetics. This would result in different flame dynamics, e.g. flame lift-off distance, the fraction of supersonic and subsonic flames. To study the different combustion modes, there are eight cases in total selected in the current work, i.e. the first group detailed in Table 3 and the second group in Table 4. Specifically, in the first simulation group, four cases, Case-A1 to Case-A4 in Table 3, share the same fuel (i.e.  $H_2$  in Table 3) injection conditions. For their air inflow conditions, the composition, Mach number and global equivalence ratio are the same as those in Case-AB. Conversely, the total temperature and static pressure increase from Case-A1 to Case-A4. Accordingly, the resultant air inflow velocities and convective Mach numbers increase in these cases.

**Table 2 – Inflow conditions of air and hydrogen in the base case, Case-AB [37].**

inlet	$u_x$ [m/s]	$T^*$ [K]	$p$ [MPa]	$Ma$	$Y_{O_2}$	$Y_{N_2}$	$Y_{H_2O}$	$Y_{H_2}$	$Ma_c$	$\phi$
air	730	600	0.1	2.0	23.2%	73.6%	3.2%	0.0	0.300	0.034
H <sub>2</sub>	1200	300	0.1	1.0	0.0	0.0	0.0	100%		

Another four cases (Case-B1 to Case-B4 in Table 4), as the second simulation group, are chosen with the same air inflow condition (same as that in Case-AB, see Table 4), but different fuel injection parameters. Recall that in the base case, i.e. Case-AB, hydrogen is injected sonically. If the air pressure is unchanged while the hydrogen pressure increases, hydrogen would be under-expanded at the injector exit. However, the maximum Mach number that hydrogen can reach at the injector exit is limited to 1.0 due to the nozzle structure [37]. Therefore, the temperature and velocity of hydrogen at the injector exit are not affected by the increased pressure.

Based on our previous investigations on the flame stabilization mechanism in this combustor using 3D LES with detailed chemistry [50], it can be confirmed that the flames in all these cases can be stabilized. Indeed, all the cases detailed in Tables 3-4 are carefully designed to avoid the possible occurrence of flame extinction based on our previous experience on this combustor [11,35,50].

## Results and discussion

### General characteristics of mixed mode combustion

Fig. 2 shows the contours of instantaneous Mach number superimposed with the iso-lines of  $Ma = 1$  for all the cases. Overall, in the first simulation group shown from Fig. 2(a)–(d) and (i), the subsonic flow regions identified by the iso-lines of  $Ma = 1$  (zone III in each figure) get shorter and narrower in the wake zone of the strut with increased air total temperature and therefore increased inflow velocity. This is schematically suggested by the long blue dashed arrow on the left half of Fig. 2. There are several isolated subsonic islands further downstream for the five cases (Case-A1 to Case-A4 and Case-AB), say beyond  $x = 240$  mm for Case-AB. Meanwhile, the evolutions of these subsonic regions are strongly unsteady, in terms of the size and spatial distribution.

In the second simulation group from Fig. 2(e)–(i), the subsonic flow regions get broader in  $y$ -direction with increased pressure of the fuel stream and therefore the global equivalence ratio. The downstream isolated subsonic islands start to

merge with the upstream continuous one. Two local subsonic bubbles are also seen at both the upper and lower combustor walls in Case-B2 and Case-B3, which are indicated by the red and blue dashed circles in Fig. 2(f) and (g), respectively. This is due to the sudden contraction of the flow area for the outer supersonic flows (in zones I and II in the figures) extruded by the inner subsonic flows (in zone III), which forms two local aerodynamic throats. These two local subsonic bubbles always occur at where for the first time in  $x$ -direction that zones I and II are narrowest and zone III is widest in  $y$ -direction. They grow in size and move upstream with higher equivalence ratios. In some extreme cases, the supersonic flows in zone I and zone II would be fully choked by the aerodynamic throats. The subsonic bubbles occupy the entire areas of zone I and zone II, and also join with zone III, i.e. the entire combustor is fully choked. This can be observed in Case-B4, in which the gas flows at low subsonic speeds below 0.5  $Ma$ . This will be further investigated in Section Critical conditions for thermal choking.

Fig. 3 shows the distributions of heat release rate per unit volume ( $q$ ) superimposed with the pink iso-lines of  $u_x = 0$  at the corresponding instant in Fig. 2 for all the cases. Overall, the length of the recirculation zone does not change significantly with increased air total temperature and global equivalence ratio (expect that in Case-B4), as respectively indicated by Line A and Line C. Furthermore, based on the time-averaged axial velocity (not shown here), the maximum mean lengths of the recirculation zone are about 50 mm (i.e. approximately ends at  $x = 160$  mm in Fig. 3) in all the simulated cases except Case-B4. However, the length of the zones with remarkable heat release rate decreases significantly with increased air total temperature in the first simulation group, as indicated by Line B. Conversely, this length increases slowly with increased global equivalence ratio in the second simulation group expect Case-B4, as indicated by Line D. As the combustor is fully choked in Case-B4, part of the combustible mixture is pushed even towards upstream of the strut, where significant heat release exists. It is found that both subsonic and supersonic flows contribute to the overall heat release when comparing Figs. 2 and 3 except Case-B4, since combustion proceeds in both supersonic and subsonic regions in these cases.

**Table 3 – Inflow conditions for the first simulation group.**

Inlet	Cases#	$Ma$	$\phi$	$T^*$ [K]	$p$ [MPa]	$Ma_c$
H <sub>2</sub>	All	1.0	–	300	1	–
Air	Case-A1	2.0	0.034	486	0.09	0.355
	Case-A2			864	0.12	0.198
	Case-A3			1176	0.14	0.104
	Case-A4			1536	0.16	0.018

**Table 4 – Inflow conditions for the second simulation group.**

Inlet	Cases#	$Ma$	$T^*$ [K]	$Ma_c$	$p$ [MPa]	$\phi$
Air	All	2.0	600	–	0.1	–
H <sub>2</sub>	Case-B1	1.0	300	0.300	0.2	0.068
	Case-B2				0.3	0.102
	Case-B3				0.35	0.119
	Case-B4				0.4	0.136

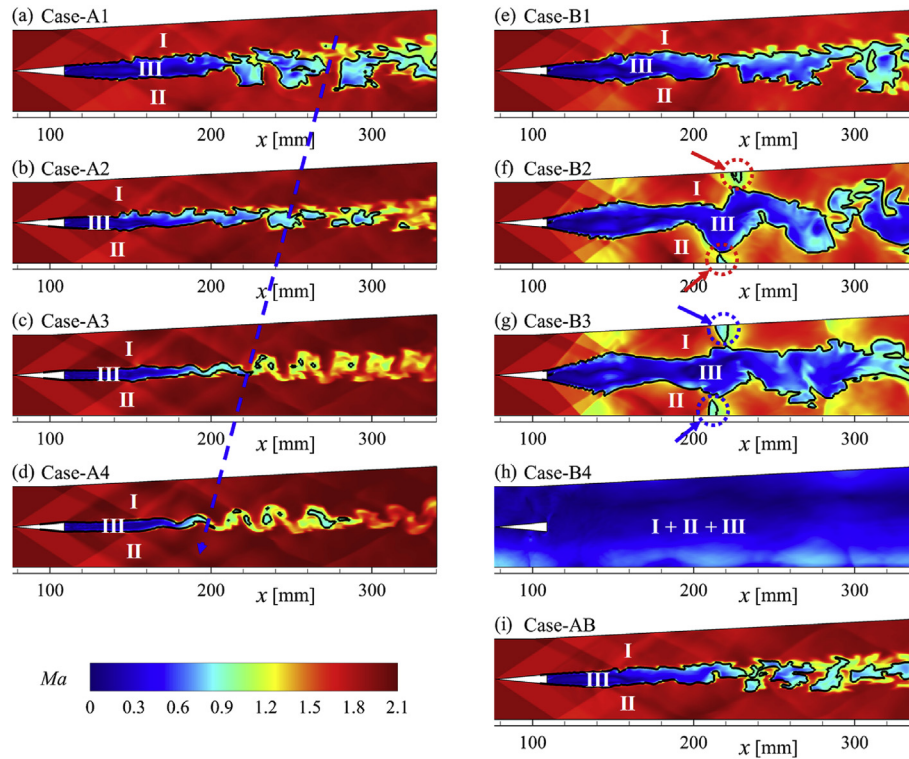


**Fig. 2** – Instantaneous contours of Mach number for all the cases. The back lines are the iso-lines of  $Ma = 1$  to identify the subsonic flow regions.

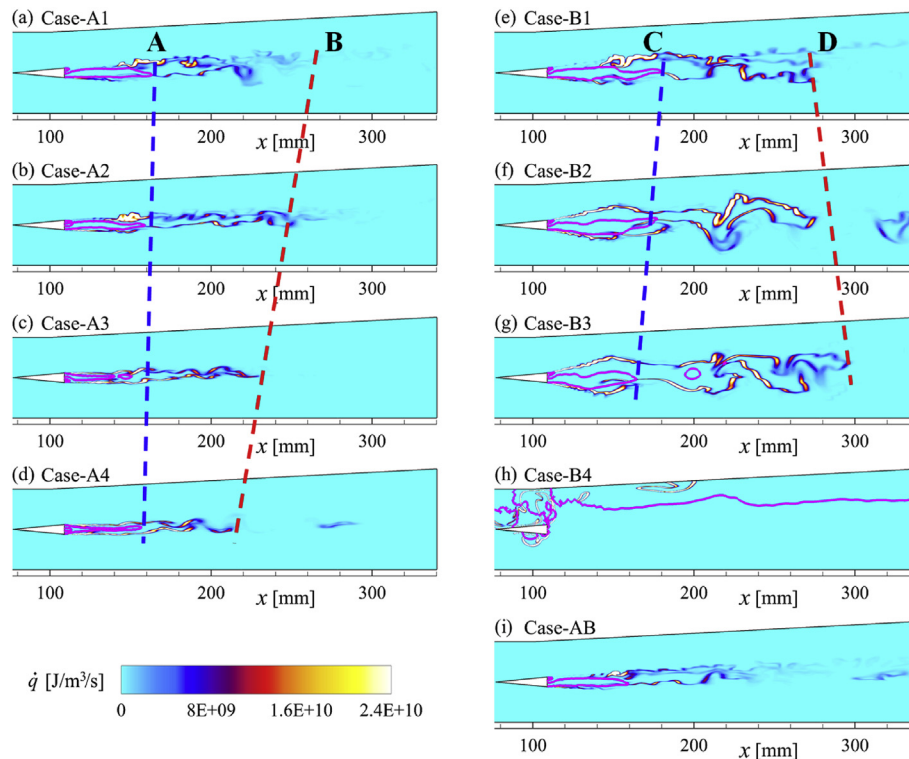


**Fig. 3** – Instantaneous contours of heat release rate per unit volume for all the cases. The pink lines are the iso-lines of  $u_x = 0$  to identify the recirculation zone. (For interpretation of the references to color in this figure legend, the reader is referred to the Web version of this article.)

To differentiate the supersonic and subsonic flows in one combustion field, a binarized metric for the local Mach number  $\xi_{Ma}$  is introduced here, which reads

$$\xi_{Ma} = \xi_{sup} + \xi_{sub}, \quad (2)$$

in which  $\xi_{sup}$  and  $\xi_{sub}$  are respectively calculated from

$$\begin{cases} \xi_{sup} = \max[\text{sign}(Ma - 1), 0] \\ \xi_{sub} = \min[\text{sign}(Ma - 1), 0], \end{cases} \quad (3)$$

where the maximum function  $\max(x, y)$  returns the larger one between  $x$  and  $y$ , whilst the minimum function  $\min(x, y)$  returns the smaller one between  $x$  and  $y$ . The sign function  $\text{sign}(x)$  returns  $+1$  if  $x \geq 0$ , and returns  $-1$  if  $x < 0$ . It is obvious from Eqs. (2) and (3) that

$$\begin{aligned} \xi_{sup} &= +1, \xi_{sub} = 0, \xi_{Ma} = +1, \text{ if } Ma \geq 1 \\ \xi_{sup} &= 0, \xi_{sub} = -1, \xi_{Ma} = -1, \text{ if } Ma < 1 \end{aligned}$$

To further differentiate the reactive gas from the non-reactive gas in the combustion field, a second metric for heat release rate (HRR),  $\xi_{Ma-\dot{q}}$ , is introduced, i.e.

$$\xi_{Ma-\dot{q}} = \xi_{sup-\dot{q}} + \xi_{sub-\dot{q}}, \quad (4)$$

where  $\xi_{sup-\dot{q}}$  and  $\xi_{sub-\dot{q}}$  are calculated from

$$\begin{cases} \xi_{sup-\dot{q}} = \xi_{sup} \cdot \max[\text{sign}(\dot{q} - \bar{q} \cdot \beta), 0] \xi_{sub-\dot{q}} \\ = \xi_{sub} \cdot \max[\text{sign}(\dot{q} - \bar{q} \cdot \beta), 0], \end{cases} \quad (5)$$

where  $\dot{q}$  is the heat release rate per unit volume,  $\bar{q}$  is the volume average of  $\dot{q}$  in the entire computational domain, and  $\beta$  is a small fraction, say 1% in this study. This value is small enough to accurately extract the reactive zones from the non-reactive zones. Based on our numerical experiments, slightly smaller or larger values of  $\beta$  would not cause any appreciable change in the results due to the sharp gradient of heat release in the combustion zone. Therefore,  $\bar{q} \cdot \beta$  can be viewed as a threshold to identify the non-zero heat release rate. It is obvious from Eqs. (3)–(5) that

$$\begin{aligned} \xi_{sup-\dot{q}} &= +1, \xi_{sub-\dot{q}} = 0, \xi_{Ma-\dot{q}} = +1, \text{ if } Ma \geq 1 \text{ and } \dot{q} \geq \bar{q} \cdot \beta \xi_{sup-\dot{q}} \\ &= 0, \xi_{sub-\dot{q}} = -1, \xi_{Ma-\dot{q}} = -1, \text{ if } Ma < 1 \text{ and } \dot{q} \geq \bar{q} \cdot \beta \xi_{sup-\dot{q}} \\ &= 0, \xi_{sub-\dot{q}} = 0, \xi_{Ma-\dot{q}} = 0, \text{ if } \dot{q} < \bar{q} \cdot \beta \end{aligned}$$

Therefore,  $\xi_{Ma-\dot{q}}$  is an indicator for various situations: supersonic flows with non-zero heat release ( $\xi_{Ma-\dot{q}} = +1$ ), subsonic flows with non-zero heat release ( $\xi_{Ma-\dot{q}} = -1$ ), and non-reactive flows ( $\xi_{Ma-\dot{q}} = 0$ ).

Fig. 4(a) and (b) compares the instantaneous distributions of  $\xi_{Ma}$  and  $\xi_{Ma-\dot{q}}$  for Case-AB. Both figures are superimposed with the white iso-lines of stoichiometric mixture fraction,  $z_{st} = 0.0282$ , which is calculated following the definition given in Ref. [38]. The two figures show different distributions of  $\xi_{Ma}$  and  $\xi_{Ma-\dot{q}}$ , e.g. in the supersonic reacting layers (denoted by the red zones in Fig. 4(b)), the recirculation zones next to the strut base (denoted by the green zones circled by the left pink ellipse I in Fig. 4(b)), and the instantaneous reaction-free subsonic bubbles (denoted by the green zones circled by the

right pink ellipse II in Fig. 4(b)). Meanwhile, it is found that almost all the iso-lines of  $z_{st}$  are located in the subsonic flow zones, which means that the recirculation zone with relatively low gas speed indeed stabilizes the flame in a supersonic incoming oxidizer. Conversely, hydrogen combustion is difficult to occur under supersonic flows for Case-AB. Although  $\xi_{Ma}$  and  $\xi_{Ma-\dot{q}}$  can respectively well distinguish the supersonic and subsonic flow or combustion regions qualitatively in space, they do not provide any quantitative information about the dominant combustion mode and the related heat release. Therefore, further investigation will be conducted in the following section on the supersonic and subsonic combustion modes and their related heat release.

### Statistics of combustion modes

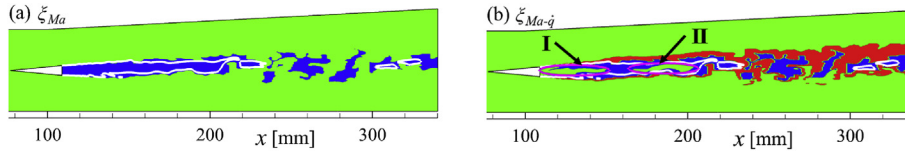
#### The averaged mach number

Fig. 5 shows the profiles of averaged Mach number along the longitudinal direction, and here the averaging is performed for different streamwise locations ( $L_y$ , in 2D case, along a line in the  $y$ -direction), i.e.

$$\bar{Ma} = \int_{L_y} Ma dy / \int_{L_y} dy. \quad (6)$$

Note that each curve in Fig. 5 starts from the strut base, i.e. at  $x = 109$  mm, and ends at the combustor exit, i.e. at  $x = 340$  mm. In the first simulation group, it shows that the averaged Mach numbers  $\bar{Ma}$  for all cases are above 1, which means that they run under supersonic mode. With increased air total temperature,  $\bar{Ma}$  increases slightly as shown in Fig. 5(a), and this may be due to the fact that the flow is more difficult to be decelerated by combustion heat release at higher inflow speeds. Moreover, less fluctuations of  $\bar{Ma}$  in the longitudinal direction are seen with increased air total temperature and therefore increased inflow velocity. The time-dependent fluctuations are less important and the flow tends to be steady at higher Mach numbers [45].

In the second simulation group,  $\bar{Ma}$  generally decreases with global equivalence ratio. This may be caused by an increased decelerating effect of combustion heat release on the gas flow at higher heat release rate. As demonstrated in Fig. 5(b), Case-B1 and Case-B4 correspond to supersonic and subsonic modes all along the streamwise direction, respectively. Nevertheless,  $\bar{Ma}$  in Case-B2 and Case-B3 shows spatially stronger fluctuations between the supersonic mode and the subsonic mode after the rear of the strut. This is due to the increased size of the subsonic flow regions with  $Ma < 1$ , leading to lower  $\bar{Ma}$  after the strut and at several downstream locations. This can be confirmed by the distributions of local Mach number in Fig. 2. The multiple transitions from  $\bar{Ma} > 1$  to  $\bar{Ma} < 1$  result in significant fluctuations of  $\bar{Ma}$  in the longitudinal direction. The larger the global equivalence ratio is, the earlier and more transition points (from  $\bar{Ma} > 1$  to  $\bar{Ma} < 1$ ) there are, and therefore the stronger fluctuations of  $\bar{Ma}$  are present. In Case-B4, in which  $\bar{Ma}$  at all points is lower than



**Fig. 4** – Comparison of instantaneous (a)  $\xi_{Ma}$  (blue:  $-1$ , green:  $+1$ ) and (b)  $\xi_{Ma-\dot{q}}$  (blue:  $-1$ , green:  $0$ , red:  $+1$ ) for Case-AB. The white lines in both (a) and (b) are the iso-lines of  $z_{st} = 0.0282$ . Ellipses I and II respectively identify the upstream and downstream non-reactive subsonic bubbles. (For interpretation of the references to color in this figure legend, the reader is referred to the Web version of this article.)

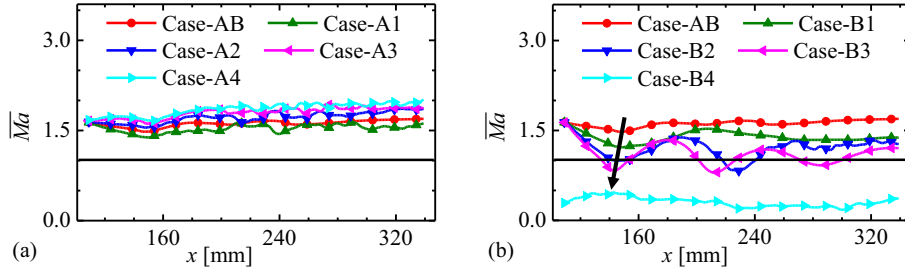


**Fig. 5** – Longitudinal profiles of averaged Mach number from (a) the first and (b) second simulation groups. The horizontal lines are the iso-lines of  $\overline{Ma} = 1$ .

1. This is in line with the qualitative observations from Fig. 2.

*The averaged mach number conditioning on heat release rate*

Fig. 6 shows the line averaged Mach number conditioning on the heat release rate along the longitudinal direction, which reads

$$\overline{Ma}_{\dot{q}} = \frac{\int_{L_y(\dot{q} \geq \bar{q})} \cdot \beta Ma dy}{\int_{L_y(\dot{q} \geq \bar{q})} \cdot \beta dy}, \quad (7)$$

where  $L_y(\dot{q} \geq \bar{q} \cdot \beta)$  denotes the regions with non-negligible heat release rate, i.e. satisfying the condition  $\dot{q} \geq \bar{q} \cdot \beta$ . It is seen that for all the cases we investigate, the combustor operates in the subsonic combustion mode, which is characterized by  $\overline{Ma}_{\dot{q}} < 1$ . Therefore, from statistical point of view, the observations from all the cases except Case-B4 are as below: a subsonic ribbon with heat release starting at the end of the strut base ( $x = 109$  mm) is embedded in the supersonic background flows with no or negligible heat release. However, Case-B4 is slightly different as flow in the combustor is fully

subsonic, as shown in Fig. 5(b). The fluctuations of  $\overline{Ma}_{\dot{q}}$  in Fig. 6 are higher than those of  $\overline{Ma}$  in Fig. 5 for the same case. This is because that the regions with non-zero  $\overline{Ma}_{\dot{q}}$  are much narrower than that with non-zero  $\overline{Ma}$ , small changes in local supersonic and subsonic combustion modes may result in significant variations in  $\overline{Ma}_{\dot{q}}$ .

*The fraction of heat release*

The fraction of heat release from supersonic and subsonic flows, denoted respectively by  $[\dot{q}_{sup}]$  and  $[\dot{q}_{sub}]$ , are also computed to quantify the dominant combustion mode. They can be estimated as below

$$\begin{cases} [\dot{q}_{sup}] = \frac{\int_{L_y(Ma \geq 1)} \dot{q} dy}{\int_{L_y} \dot{q} dy} \\ [\dot{q}_{sub}] = \frac{\int_{L_y(Ma < 1)} \dot{q} dy}{\int_{L_y} \dot{q} dy}, \end{cases} \quad (8)$$

where  $L_y(Ma \geq 1)$  and  $L_y(Ma < 1)$  in Eq. (8) are the regions with  $Ma \geq 1$  and  $Ma < 1$ , respectively. The fraction of heat release

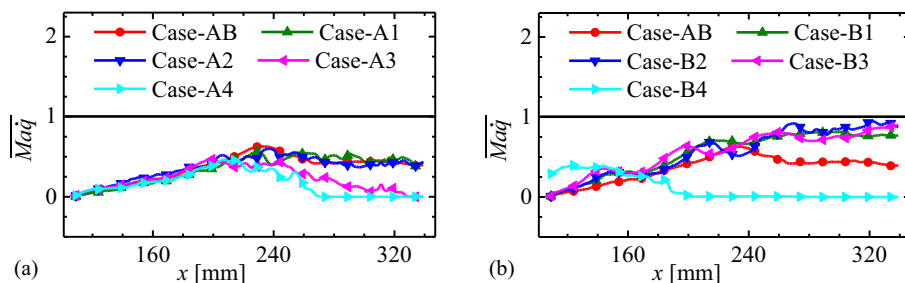


**Fig. 6** – Longitudinal profiles of averaged Mach number conditioning on heat release rate from (a) the first and (b) second simulation groups. The horizontal lines are the iso-lines of  $\overline{Ma}_{\dot{q}} = 1$ .

from supersonic combustion to the overall heat release,  $[\dot{q}_{sup}]$ , is shown in Fig. 7 for all the studied cases. It is seen that  $[\dot{q}_{sup}]$  oscillates strongly along the streamwise direction, which implies the rapid transition between supersonic heat release mode and subsonic heat release mode. With increased air total temperature in the first simulation group, the subsonic mode is dominant immediately after the strut, while the heat is mainly (>50%) from the supersonic combustion in the further downstream of the combustor. However, in the second simulation group from Fig. 7(b), with increased global equivalence ratio,  $[\dot{q}_{sup}]$  is generally below 50%, but with some fluctuations beyond that. In Case-B4, the heat is mainly released from subsonic combustion. The fluctuations of  $[\dot{q}_{sup}]$  presented in Fig. 7 are the highest than those of  $\overline{Ma}$  in Fig. 5 and  $\overline{Ma}_q$  in Fig. 6 for the same case. This is because that the variation range of HRR (generally varies from about 0 to large than  $10^{11}$  J/m<sup>3</sup>/s in our case) is much larger than that of  $Ma$  (ranges from 0 to less than 2.5).

To elucidate the distributions of the instantaneous supersonic and subsonic heat release rate,  $\dot{q}_{sup}$  and  $\dot{q}_{sub}$ , the results from Case-AB are exemplarily shown in Fig. 8. The heat release rate from supersonic and subsonic flows can be calculated respectively as

$$\begin{cases} \dot{q}_{sup} = \dot{q} \cdot \xi_{sup} \\ \dot{q}_{sub} = \dot{q} \cdot \xi_{sub} \end{cases} \quad (9)$$

$\xi_{sup}$  and  $\xi_{sub}$  are computed from Eq. (3). The first occurrence of noticeable heat release comes from the subsonic flows, at the lower end of the strut (see Fig. 8(b)). This can be justified by the fact that the flame can propagate against the subsonic flow at the outer boundary of the low speed recirculation zone. Non-zero  $\dot{q}_{sup}$  is mainly located in the upper boundary of the low-speed zone, while non-zero  $\dot{q}_{sub}$  lies in both upper and lower boundaries, as shown in Fig. 8(b). Furthermore,  $\dot{q}_{sub}$  is generally stronger and more extensive than that of  $\dot{q}_{sup}$ . With increased air total temperature in the first simulation group,  $\dot{q}_{sup}$  gets wider in space and more dominant in strength, whereas  $\dot{q}_{sub}$  gets shorter in x-direction and weaker in strength. With increased global equivalence ratio in the second simulation group,  $\dot{q}_{sup}$  gets weaker and moves towards the upper and lower combustor walls, while  $\dot{q}_{sub}$  gets more dominant in strength, longer in x-direction and broader in y-direction.

The volume integrated heat release rate from supersonic and subsonic flows,  $\dot{Q}_{sup}$  and  $\dot{Q}_{sub}$ , is respectively obtained by integrating  $\dot{q}_{sup}$  and  $\dot{q}_{sub}$  in the entire computational domain ( $S_{xy}$ ), i.e.

$$\begin{cases} \dot{Q}_{sup} = \iint_{S_{xy}} \dot{q}_{sup} dx dy \\ \dot{Q}_{sub} = \iint_{S_{xy}} \dot{q}_{sub} dx dy \end{cases} \quad (10)$$

The overall heat release rate from both modes is  $\dot{Q} = \dot{Q}_{sup} + \dot{Q}_{sub}$ . Percentages of  $\dot{Q}_{sup}$  and  $\dot{Q}_{sub}$ , respectively denoted as  $[\dot{Q}_{sup}]$  and  $[\dot{Q}_{sub}]$  as well as the value of  $\dot{Q}$  are listed in Table 5. The global combustion efficiency ( $\eta_g$ ) estimated from the ratio of  $\dot{Q}$  to the ideal heat release rate in each case is also calculated.  $\eta_{g,0}$  is  $\eta_g$  in Case-AB, and  $\eta_{g,0} \approx 98\%$ . It is found that in the first simulation group (Case-A1 to Case-A4),  $[\dot{Q}_{sup}]$  gradually increases with oxidizer total temperature, whereas  $\dot{Q}$  changes little as their fuel mass flow rates are the same. For these cases,  $\eta_g$  are close although they have different ratios of  $\dot{Q}_{sup}$  and  $\dot{Q}_{sub}$ . Therefore, the efficiency of combustion heat release in supersonic flows is as high as that in subsonic flows. This is important to achieve the desired performance of scramjet combustors operating with high speed internal flows. However, with the increased global equivalence ratio from Case-B1 to Case-B4,  $[\dot{Q}_{sup}]$  decreases while  $\dot{Q}$  increases stably. This can be speculated that more fuel injection means more heat can be released if complete combustion occurs, but stronger decelerating effect act on the flow. The efficiency  $\eta_g$  does not change significantly from Case-AB to Case-B1, i.e.  $\eta_g/\eta_{g,0}$  is about 1. However,  $\eta_g$  is reduced around 90% of  $\eta_{g,0}$  in Case-B2, Case-B3, and Case-B4, which means that the fuel H<sub>2</sub> cannot be completely consumed at the combustor exit. From the viewpoint of combustion efficiency, the operating conditions of Case-B1 are in engineering practice, as it has the highest combustion efficiency at the combustor exit among all the investigated cases.

One has seen from the above analysis that Case-A4 and Case-B4 respectively have the highest and lowest fractions of heat release from supersonic combustion. Fig. 9 further shows the joint distribution of  $\dot{q}$  versus  $Ma$  from Case-A4 and Case-B4, to account for the correspondence between flow Mach number and combustion heat release. It has been found from Table 5 that about half of the heat (approximately 58.0%) is released from subsonic flow in Case-A4. In Fig. 9, most of the scatters with high temperature lie in the range of  $Ma < 1.6$ , which contributes no more than 5% to the overall heat release. However, the scenario is different in Case-B4. The supersonic flow contributes only 6.0% to the total heat release, and therefore most heat is released in subsonic flows. Nevertheless, the highest value of  $\dot{q}$  in Case-B4 is larger than that in Case-A4.

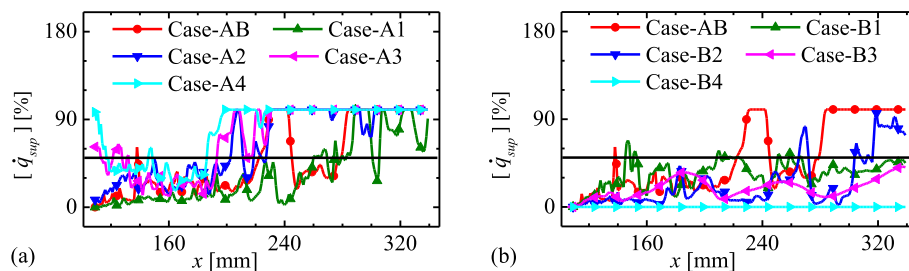


Fig. 7 – Longitudinal profiles of fraction of heat release from supersonic flows from (a) the first and (b) second simulation groups. The horizontal lines are the iso-lines of  $[\dot{q}_{sup}] = 50\%$ .

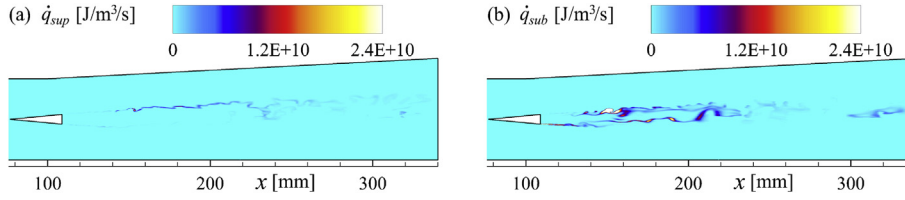


Fig. 8 – Instantaneous distributions of (a)  $\dot{q}_{sup}$  and (b)  $\dot{q}_{sub}$  for Case-AB.

Table 5 – The statistics of heat release rate from supersonic and subsonic flames.

Case #	AB	A1	A2	A3	A4	B1	B2	B3	B4
$[\dot{Q}_{sup}]$ [%]	27.4	13.1	33.2	39.2	42.0	35.0	17.3	11.9	6.0
$[\dot{Q}_{sub}]$ [%]	72.6	86.9	66.8	60.8	58.0	65.0	82.7	88.1	94.0
$\dot{Q}$ [ $10^4$ J/s]	3.53	3.41	3.41	3.49	3.33	7.18	9.58	11.31	12.65
$\eta_g/\eta_{g,0}$	1.000	0.966	0.966	0.989	0.943	1.017	0.905	0.915	0.896

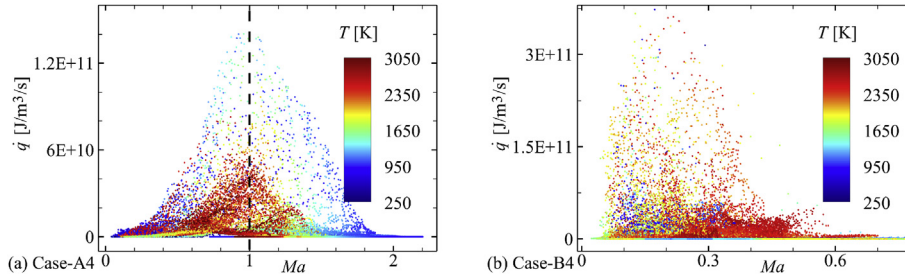


Fig. 9 – Joint distribution of local Mach number with heat release rate colored by temperature for (a) Case-A4 and (b) Case-B4. The vertical line in Fig. 9(a) is the iso-line of  $Ma = 1$ .

The probability distributions of combustion modes

According to the definition of  $\xi_{Ma-\dot{q}}$  in Eq. (4), probability density function (PDF) of different combustion modes,  $P(\xi_{Ma-\dot{q}})$ , can be written as

$$P(\xi_{Ma-\dot{q}}) = A \cdot \delta(\xi_{Ma-\dot{q}} - 1) + B \cdot \delta(\xi_{Ma-\dot{q}} + 1) + C \cdot \delta(\xi_{Ma-\dot{q}}) \quad (11)$$

where  $\delta$  is the Dirac delta function. It has the property that  $\delta(x) = \begin{cases} +\infty, & x=0 \\ 0, & x \neq 0 \end{cases}$ , and  $\int_{-\infty}^{+\infty} \delta(x) dx = 1$ . It is obvious that  $P(\xi_{Ma-\dot{q}} = +1) = \int A \cdot \delta(0) d\xi_{Ma-\dot{q}} + \int B \cdot \delta(2) d\xi_{Ma-\dot{q}} + \int C \cdot \delta(1) d\xi_{Ma-\dot{q}} = 1 \cdot A + 0 \cdot B + 0 \cdot C = A$ . It means that factor A is the probability of  $\xi_{Ma-\dot{q}} = +1$ , i.e. the probability of supersonic flamelet. Similarly, B is the probability of subsonic flamelet, and C is the probability of no flamelet. This treatment of PDF of different combustion modes, to the author's knowledge, is firstly experimentally developed by Rosenberg et al., in the study of premixed and diffusion flamelets [51].

The transient numerical simulations provide a large amount of instantaneous data to construct the PDF of different flamelets. Snapshots of the results at  $n$  different time instants are recorded after the convergence of each simulation. At any instant, there are only three possible combustion modes at each spatial position, i.e. (a) supersonic flamelet ( $\xi_{Ma-\dot{q}} = +1$ ), (b) subsonic flamelet ( $\xi_{Ma-\dot{q}} = -1$ ), and (c) no flamelet ( $\xi_{Ma-\dot{q}} = 0$ ). Assuming that at any position  $P_{ijk}$  in the computational domain, the statuses of supersonic flamelet, subsonic flamelet, and no flamelet appear  $a_{ijk}$ ,  $b_{ijk}$ , and  $c_{ijk}$  times during the  $n$  time instants. It is obvious that

$$a_{ijk} + b_{ijk} + c_{ijk} = n. \quad (12)$$

The value of  $\xi_{Ma-\dot{q}}$  at the same position  $P_{ijk}$  is summed at all the  $n$  instants, and the result is known as  $e_{ijk}$ . Therefore, we have that

$$a_{ijk} \cdot (1) + b_{ijk} \cdot (-1) + c_{ijk} \cdot (0) = e_{ijk}. \quad (13)$$

The absolute value of  $\xi_{Ma-\dot{q}}$  at the same position  $P_{ijk}$  is then summed at all the  $n$  instants, and the result is known as  $f_{ijk}$ . We have that

$$a_{ijk} \cdot |1| + b_{ijk} \cdot |-1| + c_{ijk} \cdot |0| = f_{ijk}. \quad (14)$$

Based on Eqs. 12–14, the values of  $a_{ijk}$ ,  $b_{ijk}$ , and  $c_{ijk}$  are obtained. The probability of supersonic flamelet, subsonic flamelet and no flamelet is respectively approximated as follows when the number of time instants,  $n$ , is large enough ( $n \rightarrow +\infty$ )

$$\begin{cases} A_{ijk} = P_{ijk}(\xi_{Ma-\dot{q}} = +1) = \lim_{n \rightarrow +\infty} \frac{a_{ijk}}{n} \\ B_{ijk} = P_{ijk}(\xi_{Ma-\dot{q}} = -1) = \lim_{n \rightarrow +\infty} \frac{b_{ijk}}{n}, \\ C_{ijk} = P_{ijk}(\xi_{Ma-\dot{q}} = 0) = \lim_{n \rightarrow +\infty} \frac{c_{ijk}}{n} \end{cases} \quad (15)$$

where  $A_{ijk}$ ,  $B_{ijk}$ , and  $C_{ijk}$  are the precise probability of the supersonic, subsonic, and no flamelet, while  $a_{ijk}/n$ ,  $b_{ijk}/n$ , and  $c_{ijk}/n$  are the approximate probability evaluated in the sample

space with a sample size of  $n$  time instants, at location  $P_{ijk}$ . In this study, 960 sample data in a time duration of 9.6 ms are used for each case. According to the method developed in evaluating the statistical uncertainty in Ref. [51], the statistical uncertainty using 960 snapshots is less than 3.8% with a confidence coefficient of 0.98 for Case-AB as an example. The detailed evaluation of the statistical uncertainty is provided in Appendix B.

Fig. 10 shows the probability distributions of (a) supersonic combustion mode, (b) subsonic combustion mode, and (c) no combustion, respectively, from Case-AB. High probability of supersonic flamelet can be found in the outer boundary of the hydrogen/air reaction layer, especially in the upper branch. However, that of subsonic flamelet is mainly in the combustion zone after the strut. The other regions have zero probability (no combustion occurs locally). This is consistent with the results in Figs. 3 and 8. Also note that the probability of flamelet immediately downstream of the strut is zero, which is circled by the blue ellipse in Fig. 10(c). It should be emphasized that the probability of supersonic or subsonic flamelet does not reflect the absolute amount of heat release from the corresponding combustion mode. It is seen from Fig. 8 that although heat release rate is low near the combustor exit in Case-AB, both supersonic and subsonic flamelets are all possible to occur as shown in Fig. 10.

Fig. 11 shows the statistics of  $\xi_{Ma-\dot{q}}$  in Case-AB, i.e. the average and standard deviation in the sample space. The sample average is calculated as  $\overline{\xi_{Ma-\dot{q}}} = \sum_{i=1}^n \xi_{Ma-\dot{q},i} / n$ , while the sample standard deviation is calculated as  $\sigma_{\xi_{Ma-\dot{q}}} = \sqrt{\frac{1}{n-1} \sum_{i=1}^n \xi_{Ma-\dot{q},i}^2 - \frac{n}{n-1} (\overline{\xi_{Ma-\dot{q}}})^2}$ . It is obvious that for the locations with  $\overline{\xi_{Ma-\dot{q}}} = +1$  or  $-1$ , only supersonic flamelet or subsonic flamelet can occur. At these locations, the standard deviation of  $\xi_{Ma-\dot{q}}$  is 0, since combustion mode is not changed. Indeed,  $\sigma_{\xi_{Ma-\dot{q}}}$  is an indicator of the rate of change in combustion modes. Generally, the larger  $\sigma_{\xi_{Ma-\dot{q}}}$  is, the stronger fluctuations combustion modes (supersonic, subsonic, or no combustion) have. Large values of  $\sigma_{\xi_{Ma-\dot{q}}}$  are seen at the downstream of the combustor, mainly in the transition regions between supersonic and subsonic combustion.

### Critical conditions for thermal choking

Based on the above analysis from the two simulation groups, critical value of global equivalence ratio  $\varphi_{cr}$  may exist, above which thermal choking would occur. To derive this quantity, the following assumptions are made: (a) All walls in the combustor are adiabatic and non-viscous (note that the main combustion zone in most cases locates in the central region of the combustor and is far from the walls, the heat exchange between the gas and the walls can be neglected); (b) The contribution of the  $H_2$  mass added into the combustor is ignored (e.g. in Case-AB, mass flow rate of  $H_2$  is less than 0.094% of that of air).

An infinitely small (in  $x$ -direction) control volume spanning the height of the combustor is taken in Fig. 1 (enlarged in  $x$ -direction for readability). The conservation equations for mass, momentum, and enthalpy for this control volume can be respectively written in the differential form

$$\begin{cases} \frac{d\rho}{\rho} + \frac{du_x}{u_x} + \frac{dS}{S} = 0 \\ \frac{dS}{S} + \frac{dp}{p} + k \cdot Ma^2 \cdot \frac{du_x}{u_x} = 0, \\ \dot{q} - \dot{q}_{loss} = c_p dT^* \end{cases} \quad (16)$$

where  $\rho$  is density,  $S$  is the area of the cross-plane,  $k$  is specific heat ratio,  $\dot{q}_{loss}$  is the rate of heat loss, and  $c_p$  is the specific heat capacity.

From the state equation,  $p = \rho RT$ , one obtains the following differential expression

$$\frac{dp}{p} - \frac{d\rho}{\rho} - \frac{dT}{T} = 0, \quad (17)$$

where  $R$  is the gas constant.

In high-speed duct flows, the streamwise velocity component,  $u_x$ , is generally much larger than the transverse velocity. It is satisfied that  $u_x \gg v \approx w$ , where  $v$  and  $w$  are transverse velocity components (for our 2D cases,  $w = 0$ ) [45]. Therefore,  $Ma$  is approximated as  $Ma = u_x/a$ . Substituting the definition of the speed of sound ( $a = \sqrt{kRT}$ ) into the expression  $u_x = a \cdot Ma$  yields

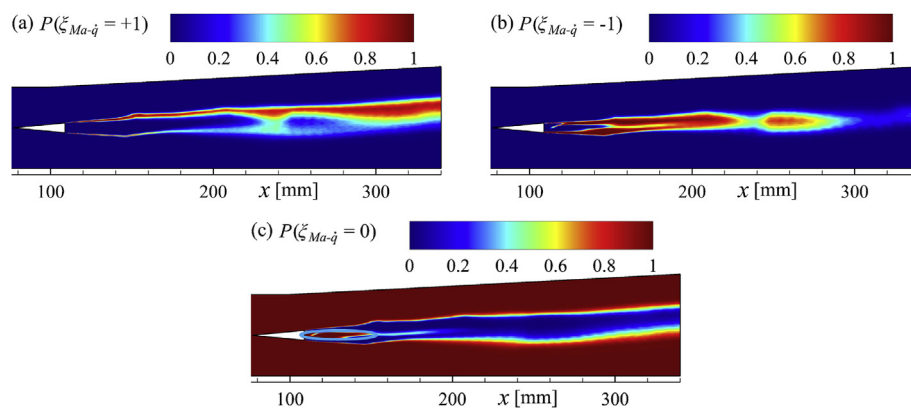


Fig. 10 – Probability distributions of (a) supersonic flamelet, (b) subsonic flamelet, and (c) no flamelet for Case-AB.

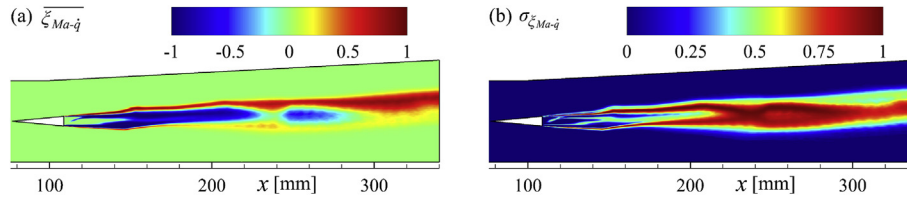


Fig. 11 – Contours of (a) average and (b) standard deviation of  $\xi_{Ma-\dot{q}}$  for Case-AB.

$$\frac{du_x}{u_x} = \frac{dMa}{Ma} + \frac{da}{a} = \frac{dMa}{Ma} + \frac{1}{2} \frac{dT}{T} \quad (18)$$

From the relation of  $T^*$  with  $Ma$ , i.e.  $T^* = T \cdot \left(1 + \frac{k-1}{2} Ma^2\right)$ , one can have

$$\frac{dT^*}{T^*} = \frac{dT}{T} + \frac{2(k-1)Ma^2}{2 + (k-1)Ma^2} \cdot \frac{dMa}{Ma} \quad (19)$$

Therefore, the relation between  $Ma$  and  $T^*$  is

$$\frac{dMa}{Ma} = \frac{(1 + k \cdot Ma^2) \cdot [2 + (k-1)Ma^2]}{4(1 - Ma^2)} \cdot \frac{dT^*}{T^*} \quad (20)$$

It shows that subsonic flow ( $Ma < 1$ ) accelerates and supersonic flow ( $Ma \geq 1$ ) decelerates with positive net heat addition ( $dT^*/T^* > 0$ ). The larger heat addition provided to the combustor, the earlier thermal choking occurs [52]. The minimum heat required to choke the combustor corresponds to the value that chokes it at the exit.

All the heat released from combustion of  $H_2$  can be approximated as a heat source with a heat power of

$$\dot{Q}_{cr} = \dot{m}_{H_2} \cdot LHV \cdot \eta_g \quad (21)$$

where  $\dot{Q}_{cr}$  is the critical heat release rate required for thermal choking,  $\dot{m}_{H_2}$  is the mass flow rate of  $H_2$ , and  $LHV$  is the lower heating value of  $H_2$ .

Meanwhile, all the heat released from combustion is assumed to increase the total enthalpy of gas when heat loss to the walls is ignored

$$\dot{Q}_{cr} = \dot{m}_{air} \cdot (c_{p,2} T_2^* - c_{p,1} T_1^*), \quad (22)$$

where  $T_1^*$  and  $T_2^*$  are the total temperatures at the combustor entrance and exit,  $c_{p,1}$  and  $c_{p,2}$  are the heat capacities at the combustor entrance and exit, respectively.  $\dot{m}_{air}$  is the mass flow rate of air inflow at the combustor entrance, which can be related to  $\dot{m}_{H_2}$  as

$$\varphi_{cr} = \frac{s \cdot \dot{m}_{H_2}}{\dot{m}_{air} \cdot Y_{O_2}^0} \quad (23)$$

Therefore, the minimum equivalence ratio for thermal choking is

$$\varphi_{cr} = \frac{s \cdot (c_{p,2} \cdot T_2^* - c_{p,1} \cdot T_1^*)}{\eta_g \cdot LHV \cdot Y_{O_2}^0} \quad (24)$$

where  $s = 8$  is stoichiometric mass ratio for  $O_2/H_2$  combustion,  $c_{p,2}$  and  $T_2^*$  can be calculated from the chemical equilibrium state of a mixture at initial temperature and pressure of the air inflow with an equivalence ratio of  $\varphi_{cr}$ . Based on Table 5,  $\eta_g$  can

be assumed to be around 90% for the choked case. Therefore, Eq. (24) provides an implicit expression to calculate  $\varphi_{cr}$  under given inflow conditions.

For the DLR combustor under the air inflow condition given in Table 2,  $\varphi_{cr}$  is 0.13. This is close to the equivalence ratio in Case-B4, which runs under the same air inflow condition as that in Table 2. Therefore, Case-B4 is theoretically predicted as a thermally choked case. This is consistent with the numerical results presented in Table 5 and in the figures shown from Figs. 5–7 for Case-B4. Indeed, from Figs. 2 and 3 it is indicated that in Case-B4 the combustor is choked, in which the Mach number is significantly smaller than 1 from  $x = 109$  mm–340 mm. Besides, Case-B3 is approaching thermal choking, as its equivalence ratio ( $\varphi = 0.119$ ) is close to  $\varphi_{cr}$ . Further increase in  $\varphi$  may lead to thermal choking and the combustion would proceed under subsonic mode, as that in Case-B4. For the other cases with equivalence ratio below  $\varphi_{cr}$ , no thermal choking is seen based on the above analysis.

The variations of  $\varphi_{cr}$  under a wider range of air inflow conditions can be further predicted with Eq. (24) as shown in Fig. 12(a), e.g. in terms of air total temperature ( $T_1^*$ ) and inflow Mach number ( $Ma_1$ ). The critical value for Case-AB is also marked for reference.  $\varphi_{cr}$  increases with  $Ma_1$  under the same  $T_1^*$ .  $\varphi_{cr}$  also increases with  $T_1^*$  under the same  $Ma_1$ , but this influence is gradually minimized when  $Ma_1$  is close to unity. Indeed, the increase of  $\varphi_{cr}$  with  $Ma_1$  and/or  $T_1^*$  is due to the increase of the corresponding air inflow velocity ( $U_{x1}$ ). Fig. 12(b) shows the variations of  $\varphi_{cr}$  with  $U_{x1}$ , and  $Ma_1$  ranges from 2.0 to 4.0. It is seen that  $\varphi_{cr}$  increases rapidly with  $U_{x1}$ . Depends on  $Ma_1$  and/or  $U_{x1}$ , thermal choking can occur under both globally fuel-lean and fuel-rich conditions. However, in all of the investigated cases, thermal choking occurs under globally fuel-lean conditions.

### Flame stability

It is found in Fig. 8 that the spatial distributions of  $\dot{q}_{sup}$  and  $\dot{q}_{sub}$  for the same case show remarkable difference, and both distributions are generally separated into two branches, i.e. the upper and lower ones. In this work, the axial location of the flame base is defined as the first occurrence of a threshold value of the reaction rate of the fuel  $H_2$ . More quantitatively, it is  $x_{FB} = \min(x | \dot{\omega}_{H_2} \leq \dot{\omega}_{H_2}^0)$ , where  $\dot{\omega}_{H_2}^0 = -60$  kg/m<sup>3</sup>/s is chosen as the threshold value. Based on our tests, choosing other threshold values of  $\dot{\omega}_{H_2}^0$ , or other quantities (e.g. temperature) would not cause obvious change of the identified flame base locations [53]. Similar to Eq. (5), the lift-off distance of supersonic and subsonic flame base is respectively estimated from

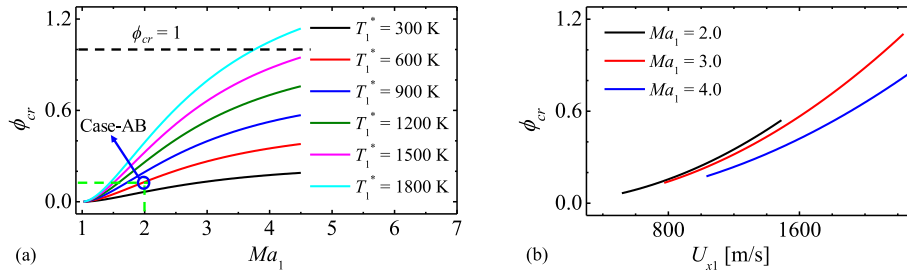


**Fig. 12 – Predicted critical equivalence ratios with respect to (a) air inflow Mach numbers at different total temperatures, and (b) air inflow velocities at different Mach numbers.**

$$\begin{cases} d_{lift-sup} = \min [x | (\dot{\omega}_{H_2} \leq \dot{\omega}_{H_2}^0) \&\& (Ma \geq 1)] - x_0 = \xi_{sup} \cdot x_{FB} - x_0 \\ d_{lift-sub} = \min [x | (\dot{\omega}_{H_2} \leq \dot{\omega}_{H_2}^0) \&\& (Ma < 1)] - x_0 = \xi_{sub} \cdot x_{FB} - x_0 \end{cases} \quad (25)$$

where  $d_{lift-sup}$  and  $d_{lift-sub}$  are the lift-off distance of supersonic and subsonic flames, respectively. Note that  $x_0 = 109$  mm is the axial location of the strut base (see Fig. 1).

It is found that at most instants, the lower branches of supersonic and subsonic flames are attached at or very close to the rear edge of the strut (e.g. as shown in Fig. 8), and hence do not show pronounced lift-off characteristics. The upper counterparts are expected to have more significant role in global flame stabilization, due to more frequent lift-off behaviors. Therefore, only the evolutions of the upper branch of supersonic and subsonic flame lift-off distance are shown in Fig. 13 with four example cases, i.e. Case-AB, Case-A1, Case-A2, and Case-B1. It is seen that the magnitude of  $d_{lift-sup}^U$  is

generally larger than that of  $d_{lift-sub}^U$  at the same instant in Case-AB, Case-A1, and Case-B1, whereas the difference is not as apparent in Case-A2. This may due to the fact that  $\dot{q}_{sup}$  is generally weaker than  $\dot{q}_{sub}$  at the same streamwise location as discussed in Fig. 8. This means that it takes longer distance for the supersonic flow to reach the same significant heat release rate as the subsonic flow does. For the one-step reaction of hydrogen we use, HRR is directly related to  $\dot{\omega}_{H_2}$ . Therefore, it generally takes longer distance for the supersonic flow to satisfy the threshold condition that we define the flame base, i.e.  $\dot{\omega}_{H_2} \leq \dot{\omega}_{H_2}^0$ .

The oscillation amplitudes of both  $d_{lift-sup}^U$  and  $d_{lift-sub}^U$  decrease when the oxidizer speed increases from Case-A1 ( $u_x = 657$  m/s), to Case-AB ( $u_x = 730$  m/s), and to Case-A2 ( $u_x = 876$  m/s). This is also true for Case-A3 and Case-A4 (not shown here). It means that the unsteady movement of both supersonic and subsonic flame fronts is suppressed at higher air inflow speeds. It has been found that combustion

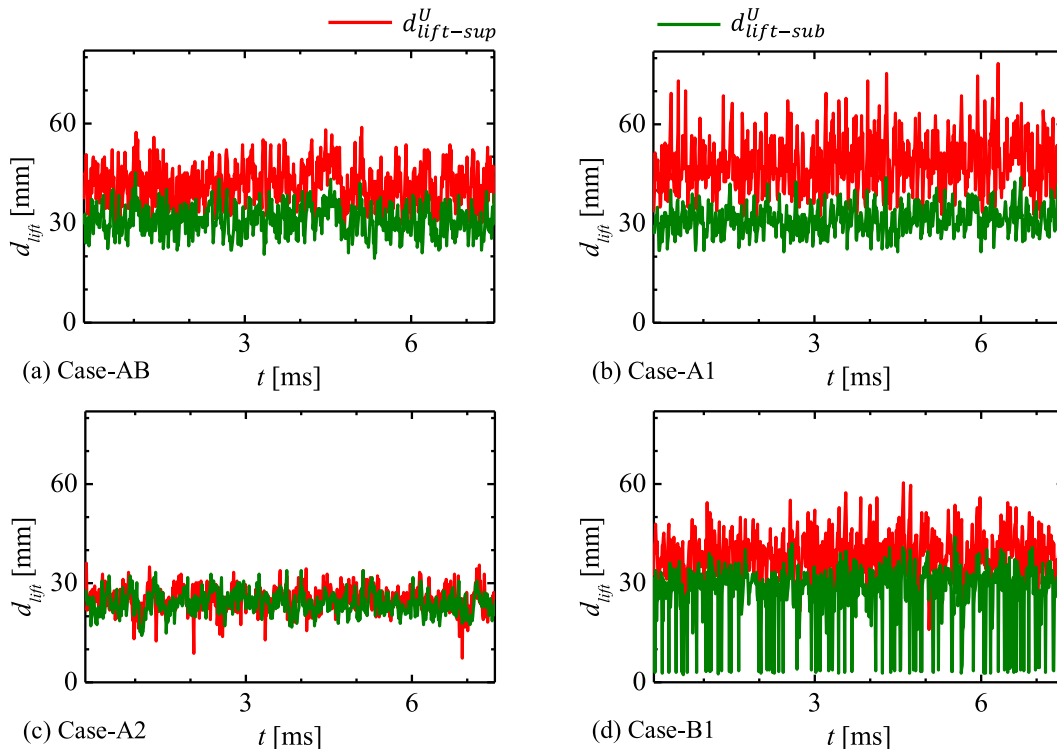


**Fig. 13 – Time evolutions of supersonic and subsonic flame lift-off distance (upper branches) for (a) Case-AB, (b) Case-A1, (c) Case-A2, and (d) Case-B1.**

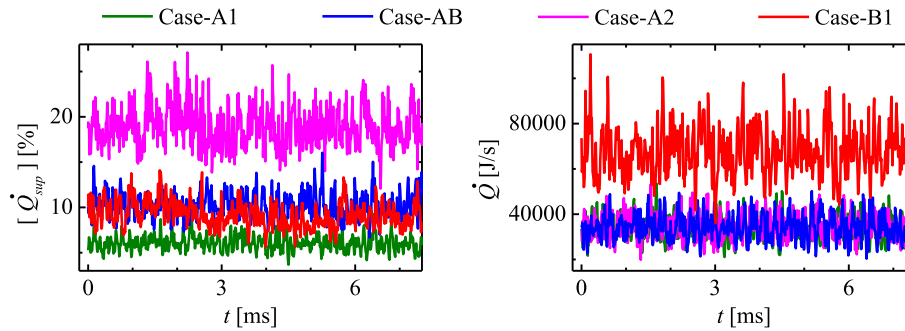


**Fig. 14** – Time evolutions of (a) percentages of volume integrated heat release rate from supersonic flames and (b) the overall heat release rate. Four cases are shown, Case-AB, Case-A1, Case-A2, and Case-B1.

oscillation in a supersonic combustor may be related to fuel/air mixing, especially when the combustor is far from thermal choking [26]. It is seen that  $Ma_c$ , which plays a dominant role in the mixing of parallel fuel/air jets, decreases consecutively from Case-A1 to Case-AB, and to Case-A2. Experimental results have indicated that a sharp reduction in shear layer growth occurs when  $Ma_c$  increases [9,54–57]. Furthermore, it is found in Fig. 3 that the mean lengths of the recirculation zone are about 50 mm in all the above four cases. Fuel mixing accomplishes in this location, and therefore, mixing efficiency in the same streamwise distance (from the rear of the strut to the end of the recirculation zone) increases dramatically from Case-A1 to Case-AB, and to Case-A2. Enhanced mixing at lower  $Ma_c$  results in suppression of combustion oscillation. Hence, both  $d_{lift-sup}^U$  and  $d_{lift-sub}^U$  decrease when air total temperature increases under the same inflow Mach number.

For Case-B1, the amplitude of  $d_{lift-sub}^U$  is obviously enhanced compared with Case-AB. This is due to the longer distance required for sufficient mixing, especially in the strut wake zone. From Figs. 2 and 3, it is found that the subsonic flame front in Case-AB and Case-B1 is limited in a region roughly bounded by  $110 \text{ mm} \leq x \leq 170 \text{ mm}$  and  $20 \text{ mm} \leq y \leq 30 \text{ mm}$ . With increased mass flow rate of  $H_2$  injected from Case-AB to Case-B1, the mixing is less homogeneous in this region and stronger subsonic combustion oscillation is resulted.

Complement to Table 5, we further extract the evolutions of heat release rate from supersonic and subsonic flames based on Eqs. 9 and 10, which reveals the instantaneous contributions of supersonic and subsonic flames to the overall heat release rate. Fig. 14(a) shows the percentages of volume integrated heat release rate from supersonic flame,  $[\dot{Q}_{sup}]$ , for the four cases shown in Fig. 13. Fig. 14(b) shows the corresponding overall heat release rate integrated in the entire computational domain. It is seen in Fig. 14(a) that  $[\dot{Q}_{sup}]$  increases statistically with increased air inflow velocity from Case-A1 to Case-AB, and to Case-A2. This is consistent with our previous analysis, i.e. higher inflow velocity leads to higher fraction of supersonic combustion. However, it is also seen that at higher inflow velocity,  $[\dot{Q}_{sup}]$  shows stronger oscillation although the oscillation of the overall heat release rate  $\dot{Q}$  does not increase noticeably as seen from Fig. 14(b). This may be due to the increased fluctuations of the subsonic bubbles at higher inflow velocity as shown in Fig. 2, which

leads to higher fluctuations of  $\dot{Q}_{sub}$  and thus  $\dot{Q}_{sup}$ . From Case-AB to Case-B1,  $[\dot{Q}_{sup}]$  decreases slightly with doubled global equivalence ratio, whereas both  $\dot{Q}$  and the oscillation of  $\dot{Q}$  almost increase twice. The decrease of  $[\dot{Q}_{sup}]$  with increased  $\phi$  may also be explained by Fig. 2, as the subsonic zones get more continuous in space with weaker fluctuations as  $\phi$  increases. The increased oscillation of  $\dot{Q}$  with  $\phi$  may be due to the more unstable spatial distribution of  $\dot{q}$  as shown in Fig. 3. The heat release zone gets more dispersive in the combustor section after the strut with increased  $\phi$ .

Similarly, we can also extract the volume of supersonic and subsonic regions, with or without heat release conditioning, to examine whether the combustor run under or close to thermal choking condition. The results are not shown here due to the length limitation. It is demonstrated that based on the separation of supersonic and subsonic flows in a mixed mode operating combustor, one can investigate both the flow dynamics (e.g. flow blockage, thermal choking) and flame dynamics (e.g. flame lift-off, heat release oscillation) independently under different flow regimes.

## Conclusions

Dynamics and statistics of mixed supersonic and subsonic combustion modes under different air inflow and global equivalence ratio conditions in a hydrogen-fueled model combustor are studied by numerical simulations in this work. Two simulation groups are selected, respectively with variable oxidizer inlet condition and fuel pressure condition (which leads to different fuel mass flow rates and therefore global equivalence ratios). Three methods are proposed for identifying supersonic and subsonic combustion modes. They include spanwise-averaged Mach number, spanwise-averaged Mach number conditioning on the local heat release, and fraction of heat release.

The results show that the subsonic flow regions in the wake zone of the strut get shorter and narrower with increased air inflow velocity, but broader and more extensive with increased global equivalence ratio. Furthermore, with the above three approaches, one can see that the transition points between the supersonic and subsonic flows, the fractions of supersonic and subsonic heat release are well

identified quantitatively. Heat release from supersonic flows increases with air inflow velocity but decreases with global equivalence ratio. The probability distributions of supersonic and subsonic combustion modes are also analyzed based on the statistics on multiple instantaneous snapshots of the results and it is shown that high probability of supersonic combustion occurs in the outer boundary of the hydrogen/air reaction layer, whereas subsonic combustion mainly occurs in the wake zone after the strut. The combustion mode changes rapidly between supersonic and subsonic at downstream of the combustor.

In addition, a critical condition for thermal choking in supersonic combustor is proposed based on the theoretical analysis on an idealized one-dimensional duct flow with heat addition. Through this, one can predict the minimum global equivalence ratio to choke a combustor under known supersonic inflow conditions. The results demonstrate that the critical equivalence ratio increases with increased inflow Mach numbers, especially with higher growth rate at higher air stagnation temperature. This is indeed due to the faster increase of air inflow velocity at higher stagnation temperatures and inflow Mach numbers. The predictions from this critical condition has been confirmed by the simulation results in this work.

Besides, it is also found that supersonic and subsonic flame base behaves differently in global flame stabilization. Specifically, the flame lift-off distance in supersonic flows is larger than that in subsonic flows. Furthermore, the oscillation amplitudes of flame lift-off distance in both supersonic and subsonic flows decrease with increased air inflow velocity, but increase with global equivalence ratio. However, the fraction of supersonic flames to the overall heat release rate as well as its fluctuations increase with increased air inflow velocity, whereas this fraction decreases while its oscillation increases with increased global equivalence ratio.

## Acknowledgments

This work was financially supported by the start-up grant by National University of Singapore (R-265-000-604-133). The simulations are performed with the computational resources from National Supercomputing Center Singapore (NSCC, <https://www.nscg.sg/>).

## Appendix A. Supplementary data

Supplementary data to this article can be found online at <https://doi.org/10.1016/j.ijhydene.2019.10.193>.

## REFERENCES

- [1] Liu C, Wang Z, Sun M, Wang H, Li P, Yu J. Characteristics of the hydrogen jet combustion through multiport injector arrays in a scramjet combustor. *Int J Hydrogen Energy* 2018;43:23511–22.
- [2] Zhang Y, Chen B, Liu G, Wei B, Xu X. Influencing factors on the mode transition in a dual-mode scramjet. *Acta Astronaut* 2014;103:1–15.
- [3] Chang J, Zhang J, Bao W, Yu D. Research progress on strut-equipped supersonic combustors for scramjet application. *Prog Aerosp Sci* 2018;103:1–30.
- [4] Sathiyamoorthy K, Danish TH, Srinivas J, Manjunath P. Experimental investigation of supersonic combustion in a strut-cavity based combustor. *Acta Astronaut* 2018;148:285–93.
- [5] Larsson J, Laurence S, Bermejo-Moreno I, Bodart J, Karl S, Vicquelin R. Incipient thermal choking and stable shock-train formation in the heat-release region of a scramjet combustor. Part II: large eddy simulations. *Combust Flame* 2015;162:907–20.
- [6] Laurence SJ, Lieber D, Martinez Schramm J, Hannemann K, Larsson J. Incipient thermal choking and stable shock-train formation in the heat-release region of a scramjet combustor. Part I: shock-tunnel experiments. *Combust Flame* 2015;162:921–31.
- [7] Park G, Park C, Jin Y, Choi H, Byun J, Hwang K. Ethylene transverse jets in supersonic crossflows. *J Propuls Power* 2015;31:773–88.
- [8] Huang W. Transverse jet in supersonic crossflows. *Aero Sci Technol* 2016;50:183–95.
- [9] Segal C. *The scramjet engine: processes and characteristics*. Cambridge, U.K.: Cambridge University Press; 2009.
- [10] Wang H, Wang Z, Sun M, Qin N. Large-Eddy/Reynolds-averaged Navier-Stokes simulation of combustion oscillations in a cavity-based supersonic combustor. *Int J Hydrogen Energy* 2013;38:5918–27.
- [11] Huang Z, He G, Wang S, Qin F, Wei X, Shi L. Simulations of combustion oscillation and flame dynamics in a strut-based supersonic combustor. *Int J Hydrogen Energy* 2017;42:8278–87.
- [12] Micka DJ, Driscoll JF. Combustion characteristics of a dual-mode scramjet combustor with cavity flameholder. *Proc Combust Inst* 2009;32(2):2397–404.
- [13] Wang H, Wang Z, Sun M, Wu H. Combustion modes of hydrogen jet combustion in a cavity-based supersonic combustor. *Int J Hydrogen Energy* 2013;38:12078–89.
- [14] Wang Y, Song W, Fu Q, Shi D, Wang Y. Experimental study of vitiation effects on hydrogen/kerosene fueled supersonic combustor. *Aero Sci Technol* 2017;60:108–14.
- [15] Ma S, Zhong F, Zhang X. Numerical study on supersonic combustion of hydrogen and its mixture with ethylene and methane with strut injection. *Int J Hydrogen Energy* 2018;43:7591–9.
- [16] Kummitha OR, Pandey KM, Gupta R. Numerical analysis of hydrogen fueled scramjet combustor with innovative designs of strut injector. *Int J Hydrogen Energy* 2018. <https://doi.org/10.1016/j.ijhydene.2018.04.067>.
- [17] Cao RF, Chang JT, Tang JF, Wang ZQ, Yu DR. Study on combustion mode transition of hydrogen fueled dual-mode scramjet engine based on thermodynamic cycle analysis. *Int J Hydrogen Energy* 2014;39:21251–8.
- [18] Noda J, Tomioka S, Sakuranaka N, Hiraiwa T. Evaluation of dual-mode combustor characteristics with vitiated and non-vitiated inflow. In: 49th AIAA/ASME/SAE/ASEE Jt Propuls Conf AIAA; 2013. AIAA 2013-3746.
- [19] Fotia ML. Mechanics of combustion mode transition in a direct-connect ramjet–scramjet experiment. *J Propuls Power* 2014;31:69–78.
- [20] Aguilera C, Yu KH. Scramjet to ramjet transition in a dual-mode combustor with fin-guided injection. *Proc Combust Inst* 2017;36:2911–8.

- [21] Huang W, Yan L, Tan JG. Survey on the mode transition technique in combined cycle propulsion systems. *Aero Sci Technol* 2014;39:685–91.
- [22] Haw WL, Goynes CP, Rockwell RD, Krauss RH, McDaniel JC. Experimental study of vitiation effects on scramjet mode transition. *J Propuls Power* 2011;27:506–8.
- [23] Bonanos AM, Schetz JA, O'Brien WF, Goynes CP. Dual-mode combustion experiments with an integrated aeroramp-injector/plasma-torch igniter. *J Propuls Power* 2008;24:267–73.
- [24] Hass N, Cabell K, Storch A, Gruber M. HiFire Direct-Connect Rig (HDCR) phase I: scramjet test results from the NASA Langley arc-heated scramjet test facility. 2012.
- [25] Yang Q, Chang J, Bao W, Deng J. A mechanism of combustion mode transition for hydrogen fueled scramjet. *Int J Hydrogen Energy* 2014;39:9791–7.
- [26] Wang ZG, Sun MB, Wang HB, Yu JF, Liang JH, Zhuang FC. Mixing-related low frequency oscillation of combustion in an ethylene-fueled supersonic combustor. *Proc Combust Inst* 2015;35:2137–44.
- [27] Huang W, Yan L. Numerical investigation on the ram-scram transition mechanism in a strut-based dual-mode scramjet combustor. *Int J Hydrogen Energy* 2016;41:4799–807.
- [28] Tian Y, Yang S, Le J. Numerical study on effect of air throttling on combustion mode formation and transition in a dual-mode scramjet combustor. *Aero Sci Technol* 2016;52:173–80.
- [29] Fureby C, Fedina E, Tegnér J. A computational study of supersonic combustion behind a wedge-shaped flameholder. *Shock Waves* 2014;24:41–50.
- [30] Oevermann M. Numerical investigation of turbulent hydrogen combustion in a SCRAMJET using flamelet modeling. *Aero Sci Technol* 2000;4:463–80.
- [31] Wang H, Shan F, Piao Y, Hou L, Niu J. IDDES simulation of hydrogen-fueled supersonic combustion using flamelet modeling. *Int J Hydrogen Energy* 2015;40:683–91.
- [32] Li Q, Wang Z. Dynamic mode decomposition of turbulent combustion process in DLR scramjet combustor. *J Aerosp Eng* 2017;30:1–10. 04017034.
- [33] Kummitha OR, Suneetha L, Pandey KM. Numerical analysis of scramjet combustor with innovative strut and fuel injection techniques. *Int J Hydrogen Energy* 2017;42:10524–35.
- [34] Wu K, Zhang P, Yao W, Fan X. Computational realization of multiple flame stabilization modes in DLR strut-injection hydrogen supersonic combustor. *Proc Combust Inst* 2019;37:3685–92.
- [35] Huang ZW, He GQ, Qin F, Wei XG. Large eddy simulation of flame structure and combustion mode in a hydrogen fueled supersonic combustor. *Int J Hydrogen Energy* 2015;40:9815–24.
- [36] Liu B, He GQ, Qin F, An J, Wang S, Shi L. Investigation of influence of detailed chemical kinetics mechanisms for hydrogen on supersonic combustion using large eddy simulation. *Int J Hydrogen Energy* 2019;44:5007–19.
- [37] Waidmann W, Alff F, Böhm M, Brummund U, Clauß W, Oswald M. Supersonic combustion of hydrogen/air in a scramjet combustion chamber. *Sp Technol* 1995;15:421–9.
- [38] Poinso T, Veynante D. Theoretical and numerical combustion. 2nd ed. Flourtown, United States: R.T. Edwards; 2005.
- [39] Greenshields CJ, Weller HG, Gasparini L, Reese JM. Implementation of semi-discrete, non-staggered central schemes in a colocated, polyhedral, finite volume framework, for high-speed viscous flows. *Int J Numer Methods Fluids* 2010;63:1–21.
- [40] Kurganov A, Tadmor E. New high-resolution central schemes for nonlinear conservation laws and convection-diffusion equations. *J Comput Phys* 2000;160:241–82.
- [41] Kurganov A, Noelle S, Petrova G. Semidiscrete central-upwind schemes for hyperbolic conservation laws and Hamilton-Jacobi equations. *SIAM J Sci Comput* 2001;23:707–40.
- [42] Zhao M, Li J-M, Teo CJ, Khoo BC, Zhang H. Effects of variable total pressures on instability and extinction of rotating detonation combustion. *Flow, Turbul Combust* 2019.
- [43] Grinstein FF, Margolin LG, Rider WJ. Implicit large eddy simulation: computing turbulent fluid dynamics. 2007.
- [44] Marinov NM, Pitz WJ, Westbrook CK, Castaldi MJ, Senkan SM. Detailed and global chemical kinetic computations for hydrogen-air mixtures. *Transp Phenom Combust* 1996. UCRL-JC-120677.
- [45] Ingenito A, Bruno C. Physics and regimes of supersonic combustion. *AIAA J* 2010;48:515–25.
- [46] Gerlinger P, Nold K, Aigner M. Influence of reaction mechanisms, grid spacing, and inflow conditions on the numerical simulation of lifted supersonic flames. *Int J Numer Methods Fluids* 2010;62:1357–80.
- [47] Berglund M, Fedina E, Fureby C, Tegnér J, Sabel'nikov V. Finite rate chemistry large-eddy simulation of self-ignition in supersonic combustion ramjet. *AIAA J* 2010;48:540–50.
- [48] Bogdanoff DW. Compressibility effects in turbulent shear layers. *AIAA J* 2008;21:926–7.
- [49] Cao D, He G, Qin F, Michaels D. Local supersonic and subsonic combustion mode transition in a supersonic jet flame. *Proc Combust Inst* 2019;37:3723–31.
- [50] Qin F, Huang Z, He G, Wang S, Wei X, Liu B. Flame stabilization mechanism study in a hydrogen-fueled model supersonic combustor under different air inflow conditions. *Int J Hydrogen Energy* 2017;42:21360–70.
- [51] Rosenberg DA, Allison PM, Driscoll JF. Flame index and its statistical properties measured to understand partially premixed turbulent combustion. *Combust Flame* 2015;162:2808–22.
- [52] Hirschel EH. Basics of aerothermodynamics. Germany: Springer Berlin Heidelberg; 2005.
- [53] Demosthenous E, Borghesi G, Mastorakos E, Cant RS. Direct numerical simulations of premixed methane flame initiation by pilot n-heptane spray autoignition. *Combust Flame* 2016;163:122–37.
- [54] Papamoschou D, Roshko A. The compressible turbulent shear layer: an experimental study. *J Fluid Mech* 1988;197:453–77.
- [55] Samimy M, Elliott GS. Effects of compressibility on the characteristics of free shear layers. *AIAA J* 1990;28:439–45.
- [56] Hall JL, Dimotakis PE, Rosemann H. Experiments in nonreacting compressible shear layers. *AIAA J* 1993;31:2247–54.
- [57] Barnes FW, Segal C. Cavity-based flameholding for chemically-reacting supersonic flows. *Prog Aerosp Sci* 2015;76:24–41.